Electrode Configurations for Piezoelectric Tube Actuators With Improved Scan Range and Reduced Cross-Coupling

Digvijay S. Raghunvanshi, Steven I. Moore, Andrew John Fleming, *Member, IEEE*, and Yuen Kuan Yong, *Member, IEEE*

***Abstract*—The article describes two new methods for driving piezoelectric tube scanners. The first method aims to maximize horizontal and vertical scan range by driving the internal electrode rather than grounding it. This approach eliminates the need for a circumferential Z-electrode, which permits longer quadrant electrodes that develop greater deflection and vertical scan range. Experimental results demonstrate a 62% increase in lateral scan range and an 87% increase in vertical scan range. The second method aims to eliminate mechanical cross-coupling between the lateral deflection, tilt angle, and vertical extension. This method involves splitting the piezoelectric tube into eight external electrodes and a driven internal electrode, similar to the first method. This configuration results in less lateral deflection but significantly reduces the tilting and vertical motion induced by lateral deflection. Experimental results demonstrate an 44% increase in vertical displacement, 96% reduction in tilting, and 62% reduction in vertical cross-coupling.**

***Index Terms*—Actuator, nanopositioning, piezoelectric tube.**

I. Introduction

PIEZOELECTRIC tube actuators are monolithic nanopositioning devices which are mechanically simple and compact. They are available at a much lower cost compared to other positioning stages such as flexure-guided nanopositioners [1]–[7]. When used as a nanopositioner, piezoelectric tubes are capable of motion in two lateral axes (X- and Y-axes) and vertical motion (Z-axes). Rotational and angular motion requires a flexure-based structure [8]. The simplicity and low cost of piezoelectric tube actuators have made them common in applications such as fiber-optic scanning [9], [10], endoscopic imaging [10]–[12], two-photon microscopy [13], [14], and atomic force microscopy [6], [15]–[17]. The schematic of a conventional tube actuator with quartered electrodes is shown in Fig. 1(a).

The piezoelectric tube actuator is a thin-walled cylinder of radially poled piezoelectric ceramic. For XYZ positioning, the standard configuration uses four external quartered electrodes and a single circumferential Z-electrode, as shown in Fig. 1(a). The internal electrode is grounded. One end of the tube is fixed and the other end is free. When voltages with equal magnitude but opposite polarity are applied to a pair of opposite quartered electrodes, e.g., $+200$ and -200 V, one side of the tube extends while the opposite side contracts, resulting in bending and lateral deflection. The magnitude of bending is approximately proportional to the applied voltage [16]. Similarly, the other pair of electrodes provide actuation in the orthogonal direction. To displace in the Z-direction, voltage is applied to the circumferential Z-electrode which is conventionally one-third of the tube length and located at the free-end of the tube.

This article proposes an alternative configuration method actuation where the internal electrode is driven with a negative voltage (V_i) rather than connecting it to ground. This approach eliminates the need for a circumferential Z-electrode which simultaneously allows longer quadrant electrodes, and allows the entire tube length to generate vertical displacement. To avoid exceeding the coercive field strength of the material, the internal voltage is restricted to a negative polarity. It should be noted that the maximum electric field in the poling direction is doubled by the proposed method. However, this is typically five times the coercive field strength; so the resulting electric field is less than half of the limiting value. The proposed actuation method is applied to a piezoelectric tube with full-length quartered electrodes as shown in Fig. 1(b).

A disadvantage of the standard drive method described above is tilting of the moving platform which is proportional to deflection. The tilt angle distorts the interference pattern in optical microscopy [18] and reduces image quality in atomic force microscopy [19]. To reduce the tilt angle, an eight-electrode tube actuator is proposed where the outer electrodes are split to create upper and lower sections. When applying voltages with the same magnitude on the X- or Y-electrode but with opposite polarity at the two halves, the tube bends in a sigmoid shape which reduces the tilt angle significantly. However, the deflection range is approximately halved, as described in Section II-B. In [19],

Manuscript received June 8, 2018; revised May 12, 2019 and October 22, 2019; accepted January 24, 2020. Date of publication March 4, 2020; date of current version June 15, 2020. Recommended by Technical Editor Prof. Q. Zou. This work was supported by the Australian Research Council. (Corresponding author: Yuen Kuan Yong.)

The authors are with the School of Electrical Engineering and Computing, University of Newcastle, Callaghan, NSW 2308, Australia (e-mail: digvijay.raghuvanshi@uon.edu.au; steven.i.moore@uon.edu.au; andrew.fleming@newcastle.edu.au; yuenkuan.yong@newcastle.edu.au).

Color versions of one or more of the figures in this article are available online at http://ieeexplore.ieee.org.

Digital Object Identifier 10.1109/TMECH.2020.2978241

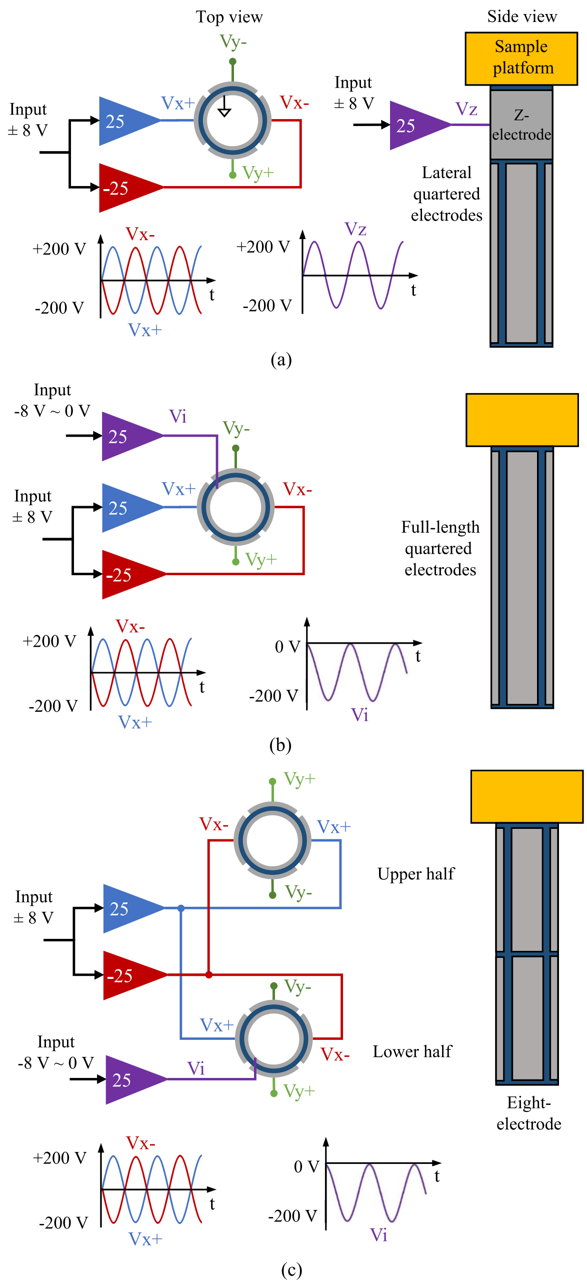

Fig. 1. Electrode configuration and driving method for the (a) conventional, (b) full-length, and (c) eight-electrode piezoelectric tube actuators.

voltage is applied to the outer circumferential Z-electrode of the eight-electrode tube to generate vertical displacement. This article proposes to eliminate the Z-electrode by driving the inner electrode with a negative voltage, as illustrated Fig. 1(c). This approach utilizes the entire length of the tube to generate vertical extension which significantly increases the range. Eliminating the Z-electrode also allows longer and perfectly symmetrical quadrant electrodes, which increases range and eliminates both tilting and cross-coupling between lateral and vertical motion.

To evaluate the performance of the proposed drive configurations shown in Fig. 1(b) and (c), the displacements and cross-coupling motions are compared to the conventional

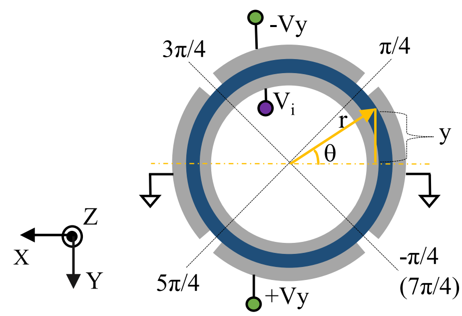

Fig. 2. Cross-section of the tube in the *XY* plane. The Y-electrodes are driven with equal but opposite voltages V_y, and the internal electrode is driven by V_i. The X-electrodes are grounded.

configuration shown in Fig. 1(a). All three tubes have identical dimensions, that is, 50.8 mm length, 0.66 mm thickness, and an 9.5 mm outer diameter.

The rest of this article is organized as follows. Section II presents a detailed deflection analysis of the full-length and eight-electrode piezoelectric tubes. The modeling also establishes that the voltage V_i applied to the inner electrode only affects vertical displacement. Section III compares the finite-element (FE) simulations of each configuration using ANSYS. Experimental results are presented and compared in Section IV. Section V concludes this article.

II. Analytical Deflection Estimations

A. Full-Length Piezoelectric Tube Actuator

This section derives the deflection of the full-length tube, as described in Fig. 1(b), based on the Euler–Bernoulli equations. To produce lateral deflection along the Y-axis, the Y-electrodes are driven differentially with $\pm V_y$ Volts as shown in Fig. 2. The X-electrodes are grounded and the internal electrode is actuated with V_i Volts. Lateral deflection along the X-axis can be derived similarly by applying differential voltages to the X-electrodes.

In the following, polar co-ordinates (z, r, θ) are employed for convenience. The transformation $(x, y) = (-r\cos\theta, -r\sin\theta)$ converts Cartesian co-ordinates to polar co-ordinates. In the polar co-ordinates, the applied voltage $V(\theta)$ is

$$V(\theta) = \begin{cases} -V_y - V_i & \theta \in (\pi/4, 3\pi/4) \\ V_y - V_i & \theta \in (5\pi/4, 7\pi/4) \\ 0 & \text{otherwise} \end{cases}. \quad (1)$$

Applying Euler–Bernoulli kinematic assumptions [20], the strain S_1 is

$$S_1(z, r, \theta) = -r\sin(\theta)w''(z) \quad (2)$$

where (z, r, θ) are cylindrical co-ordinates and $w(z)$ is the lateral deflection as a function of z. In this problem the tube is assumed thin and thus r is the tube's outer radius. In the Euler–Bernoulli beam, all other strains are zero. The constitutive equations of the piezoelectric material are

$$T_1 = ES_1 - e_{31}E_3 \quad (3)$$

$$D_3 = e_{31}S_1 + \varepsilon_{33}E_3 \tag{4}$$

where T_1 is the stress, E is the elastic modulus, e_{31} is the piezoelectric coefficient, E_3 is the electric field, D_3 is the electric displacement, and ε_{33} is the permittivity. Assuming a thin tube structure, the electric field is a function of voltage given by

$$E_3 = V(\theta)/h \tag{5}$$

where h is the thickness of the tube. Substituting (2) and (5) into (3) results in the following expression for the stress around the circumference of the tube

$$T_1 = -Er\sin(\theta)w''(z) - e_{31}V(\theta)/h. \tag{6}$$

The first part of this expression is the stress caused by the mechanical structure and the second part is the stress due to the piezoelectric effect. These stresses induce moments which cause the cross-sectional area to rotate around the neutral axis. Assuming there is no net axial force on the structure, the total moment on the cross-sectional area is

$$M = \int_0^{2\pi} yT_1 \mathrm{d}\theta \tag{7}$$

where $y = -r\sin(\theta)$ as shown in Fig. 2. Substituting (1) and (6) into (7) gives,

$$\begin{aligned} M &= \int_0^{2\pi} -r\sin(\theta)T_1 \mathrm{d}\theta \\ &= \int_{-\pi/4}^{\pi/4} E\kappa^2\, w''(z)d\theta \\ &\quad + \int_{\pi/4}^{3\pi/4} \left[E\kappa^2\, w''(z) + e_{31}\kappa\frac{(-V_y - V_i)}{h}\right] d\theta \\ &\quad + \int_{3\pi/4}^{5\pi/4} E\kappa^2\, w''(z)d\theta \\ &\quad + \int_{5\pi/4}^{7\pi/4} \left[E\kappa^2\, w''(z) + e_{31}\kappa\frac{(V_y - V_i)}{h}\right] d\theta \end{aligned} \tag{8}$$

where $\kappa = r\sin(\theta)$. Solving the above integration gives

$$\begin{aligned} M &= Er^2\, w''(z)\pi + \frac{\sqrt{2}e_{31}r}{h}(-V_y - V_i - V_y + V_i) \\ &= Er^2\, w''(z)\pi - \frac{2\sqrt{2}e_{31}rV_y}{h} \end{aligned} \tag{9}$$

Note that the voltage of the inner electrode (V_i) is eliminated in the above expression, indicating the internal driving voltage has no effect on the lateral deflection of the tube. With no external load, the net moment is zero when in equilibrium, that is

$$M = Er^2\, w''(z)\pi - \frac{2\sqrt{2}e_{31}rV_y}{h} = 0. \tag{10}$$

Rearranging the above equation and substituting $r = D/2$ and $e_{31} = Ed_{31}$ gives

$$w''(z) = \frac{4\sqrt{2}d_{31}V_y}{hD\pi} \tag{11}$$

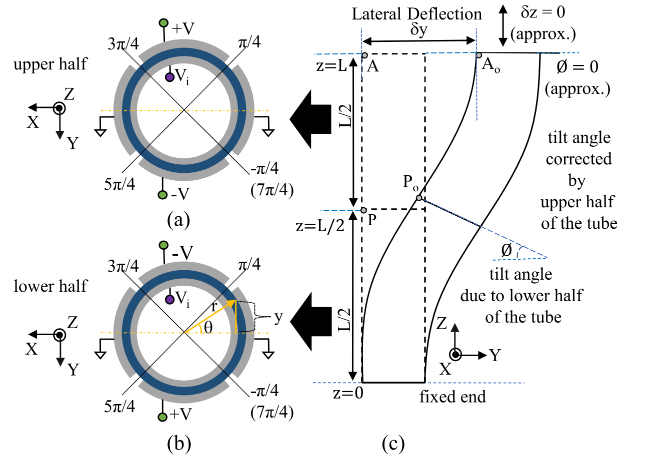

Fig. 3. Y-electrodes are driven with $\pm V_y$ in the upper and lower half of the tube. The internal electrode is driven with V_i. The X-electrodes are connected to ground.

where, d_{31} is the piezoelectric strain constant and D is the tube diameter.

To obtain an expression for the lateral deflection, double integration is performed on (11) with the boundary conditions $w'(z) = 0$ at $z = 0$, and $w(z) = 0$ at $z = 0$. The deflection of the tube at $z = L$ is

$$w(L) = \delta_y = \frac{2\sqrt{2}d_{31}L^2V_y}{\pi Dh} \tag{12}$$

which is identical to that derived by Chen [21].

For vertical motion, the standard deflection equation is used

$$\delta_z = \frac{d_{31}LV_i}{h}, V_i < 0. \tag{13}$$

In the conventional configuration, where the x and y electrodes only cover a percentage of the length, the total displacement is the sum of the active length L_y displacement and the passive length L_p deflection. The deflection of the passive length can be found by integrating (11) to obtain tube slope at the end of the active electrode

$$w'(L_y) = \frac{4\sqrt{2}d_{31}V_y}{hD\pi}L_y. \tag{14}$$

Then the deflection of the passive length is $w'(L_y)L_p$, and the total deflection is

$$\delta_y = \frac{2\sqrt{2}d_{31}L_y^2V_y}{\pi Dh} + w'(L_y)L_p. \tag{15}$$

B. Eight-Electrode Piezoelectric Tube Actuator

The eight-electrode tube is also modeled using Euler–Bernoulli beam theory. To develop deflection along the Y-axis, the upper and lower pairs of the quartered Y-electrodes are actuated with $\pm V_y$ Volts and the internal electrode is actuated with V_i Volts as described in Fig. 3. The X-electrodes are grounded.

The voltage $V(z,\theta)$ applied is

$$V(z,\theta) = \begin{cases} -V_y - V_i, & \theta \in \left(\frac{\pi}{4}, \frac{3\pi}{4}\right), \quad z < \frac{L}{2} \\ V_y - V_i, & \theta \in \left(\frac{5\pi}{4}, \frac{7\pi}{4}\right), \quad z < \frac{L}{2} \\ V_y - V_i, & \theta \in \left(\frac{\pi}{4}, \frac{3\pi}{4}\right), \quad z > \frac{L}{2} \\ -V_y - V_i, & \theta \in \left(\frac{5\pi}{4}, \frac{7\pi}{4}\right), \quad z > \frac{L}{2} \\ 0, & \text{otherwise} \end{cases}. \tag{16}$$

For a thin tube, a parallel plate capacitive structure is used to approximate the electric field distribution in the tube. The radial electric field $E_3(z,r,\theta) = V(z,\theta)/h$, where h is the thickness of the tube. Applying Euler–Bernoulli kinematic assumptions [20], the strain is

$$S_1(z,r,\theta) = -r\sin(\theta)w''(z) \tag{17}$$

where $w(z)$ is the lateral deflection. Due to the split in the outer electrode at $z = \frac{L}{2}$, $w''(z)$ is evaluated for the upper and lower sections separately

$$w''(z) = \begin{cases} w_1''(z) & z \in (0, \frac{L}{2}) \\ w_2''(z) & z \in (\frac{L}{2}, L) \end{cases}. \tag{18}$$

Substituting $E_3(z,r,\theta)$ and $S_1(z,r,\theta)$ into (3) results in the following expression for the stress in the tube

$$T_1(z,r,\theta) = -Er\sin(\theta)w''(z) - e_{31}V(z,\theta)/h. \tag{19}$$

The first term of this expression is the stress exerted by the material and the second term is the stress due to the piezoelectric effect. These stresses induce moments about the neutral axis of the tube. The total moment on the cross-sectional area is

$$M(z) = \int_\Omega yT_1 \mathrm{d}\Omega \tag{20}$$

where the domain Ω is the cross sectional area of the tube. $M(z)$ is evaluated for upper and lower sections separately

$$M(z) = \begin{cases} M_1(z) & z \in (0, \frac{L}{2}) \\ M_2(z) & z \in (\frac{L}{2}, L) \end{cases}. \tag{21}$$

For a thin tube of radius r, $y = -r\sin(\theta)$, therefore $M_1(z)$ is evaluated as

$$\begin{aligned} M_1(z) &= \int_\theta -r\sin(\theta)T_1 \mathrm{d}\theta \\ &= Er^2w_1''(z)\pi + \frac{\sqrt{2}e_{31}r}{h}(-V_y - V_i - V_y + V_i) \\ &= Er^2w_1''(z)\pi - \frac{2\sqrt{2}e_{31}rV_y}{h}. \end{aligned} \tag{22}$$

Similar evaluation for $M_2(z)$ gives

$$M_2(z) = Er^2w_2''(z)\pi + \frac{2\sqrt{2}e_{31}rV_y}{h}. \tag{23}$$

Note that the voltage V_i of the inner electrode is eliminated in the moment expression which shows that V_i has no effect on the lateral displacement of the tube. With no external load, the net moment on the cross-sectional area is zero when in equilibrium and is evaluated in the upper and lower sections as

$$M_1(z) = Er^2w_1''(z)\pi - \frac{2\sqrt{2}e_{31}rV_y}{h} = 0 \tag{24}$$

$$M_2(z) = Er^2w_2''(z)\pi + \frac{2\sqrt{2}e_{31}rV_y}{h} = 0. \tag{25}$$

Rearranging and substituting $r = D/2$ and $e_{31} = Ed_{31}$, where D is the diameter, and d_{31} is the piezoelectric strain constant, the above equations give

$$w_1''(z) = \frac{4\sqrt{2}d_{31}V_y}{hD\pi}, \quad w_2''(z) = -\frac{4\sqrt{2}d_{31}V_y}{hD\pi}. \tag{26}$$

Integrating w_1''

$$w_1'(z) = \phi_1(z) = Kz + C \tag{27}$$

$$w_1(z) = \frac{z^2\ K}{2} + C_1z + C_2 \tag{28}$$

where $K = 4\sqrt{2}d_{31}V_y/(hD\pi)$ and $\phi_1(z)$ is the angle. Applying boundary conditions $w_1'(0) = 0$ and $w_1(0) = 0$ results in $C_1 = 0$ and $C_2 = 0$. Similarly integrating w_2'' gives

$$w_2'(z) = \phi_2(z) = -Kz + C_3 \tag{29}$$

$$w_2(z) = -\frac{z^2\ K}{2} + C_3z + C_4. \tag{30}$$

Applying boundary conditions $w_1'(\frac{L}{2}) = w_2'(\frac{L}{2})$ and $w_1(\frac{L}{2}) = w_2(\frac{L}{2})$ results in $C_3 = KL$ and $C_4 = -\frac{KL^2}{4}$. Substituting these constants into w_2, the deflection of the eight-electrode tube actuator at $z = L$ is

$$\delta_y = w_2(L) = \frac{\sqrt{2}d_{31}L^2V_y}{\pi Dh}. \tag{31}$$

That is, the deflection of the eight-electrode configuration is half that of the four-quadrant configuration [21]. This is the tradeoff required to eliminate tilting and cross-coupling. Similarly, the deflection equation in the X-axis is

$$\delta_x = \frac{\sqrt{2}d_{31}L^2V_x}{\pi Dh}. \tag{32}$$

For vertical motion, the standard axial extension equation is

$$\delta_z = \frac{d_{31}LV_i}{h} \tag{33}$$

where V_x, V_y, and V_i are the magnitudes of electrode voltages for the X-, Y-, and Z-axis, respectively. In the experimental setup, the voltages V_x and V_y and are kept in the range [−200, 200] and V_i is in the range [−200, 0]. Analytical deflections of the conventional, full-length, and eight-electrode tubes calculated using (12)–(13) and (31)–(33) are provided in Table III.

III. Finite-Element Analysis

A FE analysis is performed to compare the maximum deflection δ_x, δ_z, cross-coupling from X to ϕ, and cross-coupling from X to d_z, of each electrode configuration. All three tubes are made of PZT-5H piezoelectric ceramic material having length

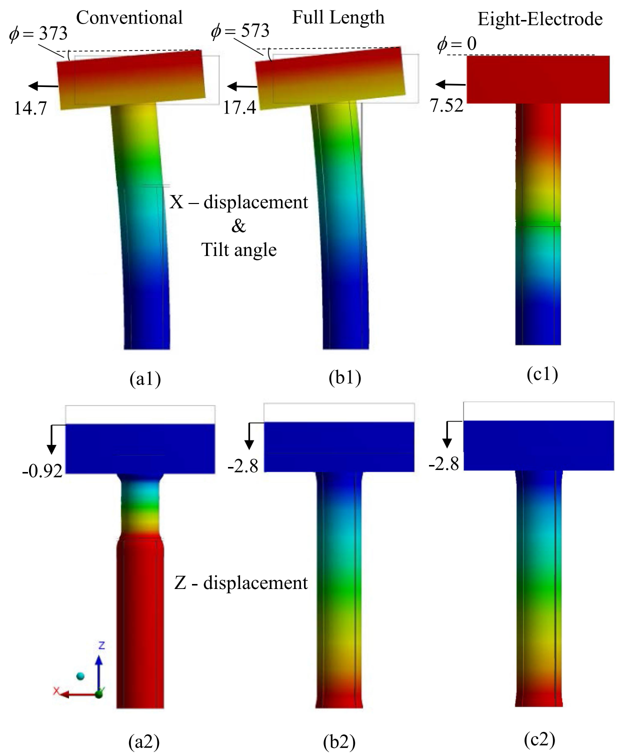

Fig. 4. FE simulated deflections (in μm) and tilt angle (in μrad) of the (a) conventional, (b) full-length, and (c) eight-electrode piezoelectric tube actuators.

TABLE I
PIEZOELECTRIC PROPERTIES OF THE TUBE ACTUATORS

Piezoelectric coeff. (C/m^2)			Relative permittivity ϵ^S/ϵ_o		Piezoelectric const. ($\times 10^{-12}$m/V)
e_{31}	e_{33}	e_{15}	ϵ_{11}	ϵ_{33}	d_{31}
-6.55	23.3	17.0	1700	1470	-274

TABLE II
VOLTAGES APPLIED TO THE FE MODELS TO DEVELOP LATERAL AND VERTICAL DEFLECTION

Tube	Def.	$V_{X+/-}$	$V_{Y+/-}$	V_i	V_z
Conventional	δx	± 200	0	0	0
Conventional	δz	0	0	0	± 200
Full-length	δx	± 200	0	0	N/A
Full-length	δz	0	0	-200	N/A
Eight-electrode	δx	± 200	0	0	N/A
Eight-electrode	δz	0	0	-200	N/A

50.8 mm, thickness 0.66 mm, and outer diameter 9.5 mm. ANSYS workbench with the PiezoAndMEMS extension is used to conduct the FE modeling as shown in Fig. 4. For the conventional tube, the length of the outer circumferential Z-electrode is one-third of the length, and the quadrant electrodes are two-thirds of the length. An aluminium holder which serves as a sensor target in experiments is also modeled. Table I lists the piezoelectric material properties in stress form (e). A cylindrical co-ordinate system is used to define the polarization vector, which is orientated radially inward. Input voltages are applied to the three tube actuators as illustrated in Fig. 1. Table II lists the actuation voltages applied to each electrode configuration.

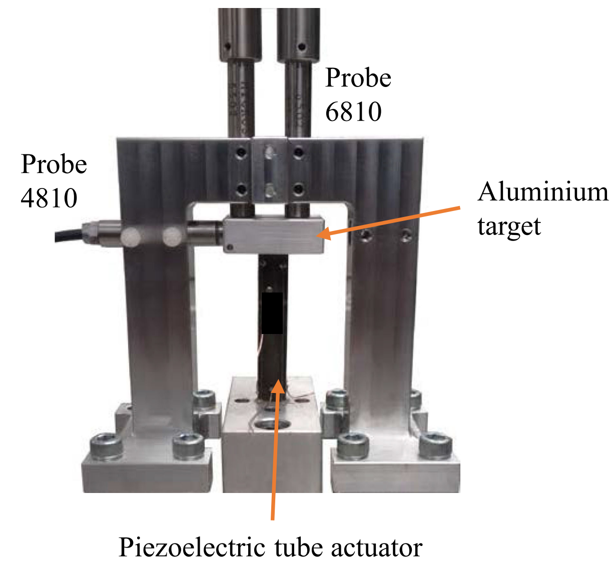

Fig. 5. Experimental setup.

FE simulation results are summarized in Table III. The full-length configuration exhibits an 18% increase in lateral scan range and 52% increase in vertical scan range compared to the conventional electrode configuration. The normalized cross-couplings, ϕ/δ_x and δ_z/δ_x, are also increased by about 30% and 35%, respectively, primarily due to the increase in the tilt angle and a larger strain experienced by the tube.

Table III also reports the vertical travel range per mm of vertical electrode (δ_z/L_z). Since the full-length and eight-electrode configurations are limited to negative voltages on the internal electrode, the travel range per mm of electrode length is half that of the conventional tube. However, since the effective electrode length of the full-length and eight-electrode configurations is longer, the overall vertical travel range is greater (assuming the vertical electrode length is less than half the tube length).

For the eight-electrode tube, the lateral scan range is reduced by 49% and 57% compared to the conventional and full-length tube, respectively. However, the eight-electrode tube shows negligible vertical and tilting motion induced by lateral deflection. The vertical scan range of the eight-electrode tube is also increased by 52% compared to the conventional tube due to the driven internal electrode.

Since the electrode configurations do not alter the resonance frequencies or mode shapes [22], they are not studied in this work. However, it can be noted that eliminating the circumferential electrode can reduce the tube length and increase resonance frequency [22].

IV. EXPERIMENTS

Fig. 5 shows the experiment setup for displacement measurement of the three tubes. Two MicroSense 6810 capacitive sensors are used to measure the vertical displacement δ_z and the tilt angle ϕ. A MicroSense 4810 capacitive sensor is used to measure the lateral deflection δ_x. All three sensors have a sensitivity of 10 μm/V. The bandwidth of the three sensors are

TABLE III
ANALYTICAL, FE, AND EXPERIMENTAL RESULTS COMPARING THE MAXIMUM DEFLECTION AND CROSS-COUPLING OF THE THREE ELECTRODE CONFIGURATIONS

Axis Driven	Deflection	Analytical			FE Simulations			Experimental Results		
		Conv.	Full-length	8-elect.	Conv.	Full-length	8-elect.	Conv.	Full-length	8-elect.
X	δ_x (μm)	$\pm$18.1	$\pm$20.3	$\pm$10.1	$\pm$22.35	$\pm$24.0	$\pm$10.1	$\pm$26.24	$\pm$42.4	$\pm$14.73
	ϕ (μrad)	–	–	–	$\pm$507.07	$\pm$763.02	$\pm$27.56	$\pm$740.6	$\pm$1486.7	$\pm$17.1
	δ_z (μm)	–	–	–	-0.0048	-0.0088	-0.00076	-0.0279	-0.0635	-0.006
	$\lvert\phi/\delta_x\rvert$ (rad/m)	–	–	–	22.7	31.8	2.73	28.22	35.06	1.16
	$\lvert\delta_z/\delta_x\rvert$ ($\times 10^{-3}$)	–	–	–	0.22	0.36	0.03	1.06	1.50	0.41
Z	δ_z (μm)	$\pm$1.41	-4.22	-4.22	$\pm$1.31	-3.8	-3.8	$\pm$1.81	-6.77	-5.22
	δ_z/L_z (μm/mm)	0.167	0.0831	0.0831	0.154	0.0748	0.0748	0.213	0.133	0.103

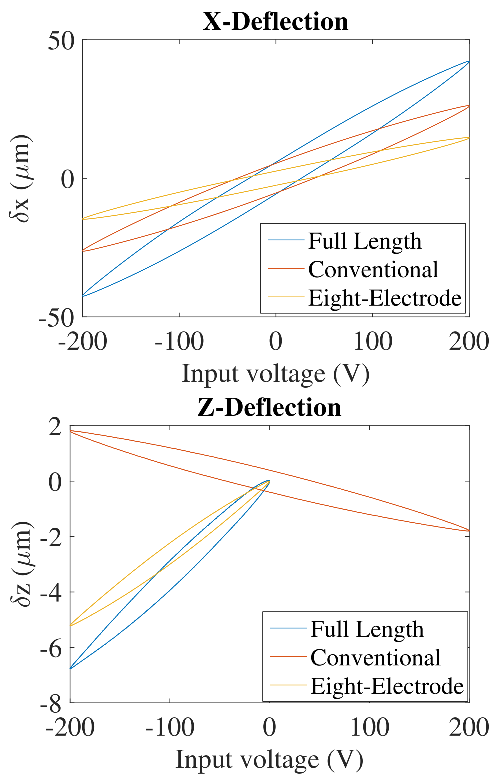

Fig. 6. Measured deflections, δ_x and δ_z, for the conventional, full-length and eight-electrode piezoelectric tube actuators.

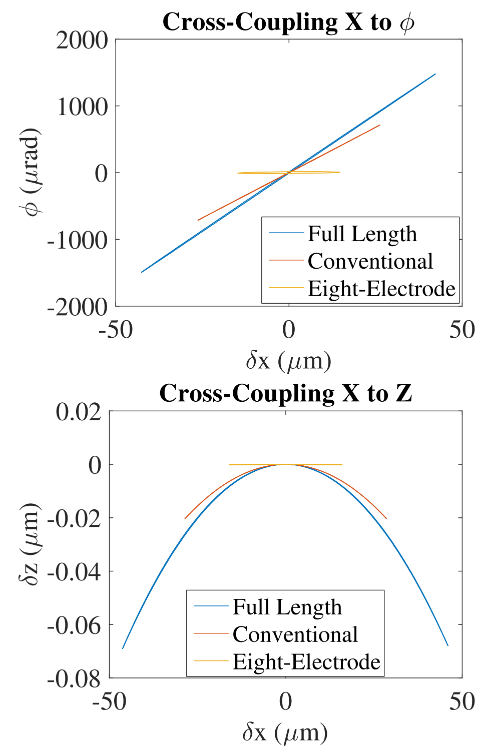

Fig. 7. Measured cross-coupling motions from X to ϕ and from X to Z.

set to 10 kHz. A PiezoDrive TD250 high-voltage amplifier with a gain of 25 V/V is used to drive the piezoelectric tube actuators. A dSPACE MicroLabBox prototyping system which has a sampling rate of 80 kHz are used to generate the input signals and records the sensor measurements. To generate X-displacement, a 1-Hz sinusoidal signal is amplified to $\pm$ 200 V. For both the eight-electrode and full-length tube actuators, negative voltages in the range of -200 to 0 V are applied to their inner electrode to produce vertical displacement. For the conventional tube, the circumferential Z-electrode is driven with $\pm$ 200 V while keeping the internal electrode at ground to produce Z-displacement.

The measured displacement and cross-coupling of the three tubes is compared in Table III and plotted in Figs. 6 and 7. Compared to the conventional electrode configuration, the full-length electrode configuration exhibits a 62% increase in the lateral scan range and a 87% increase in the vertical scan range. The normalized cross-couplings ϕ/δ_x and δ_z/δ_x are also increased by 24% and 41%, respectively, as there are proportional to the lateral range.

For the eight-electrode configuration, the lateral scan range is 44% less than the conventional configuration. However, the normalized tilting ϕ/δ_x and vertical cross-coupling δ_z/δ_x are reduced by 96% and 43%, respectively. The proposed actuation method increases the δ_z range by 44% compared to that of the conventional electrode configuration. Although the eight-electrode configuration has the same length as the full-length configuration, there is a discrepancy in the measured δ_z due to different inner electrode lengths caused by manufacturing imperfections.

The hysteresis of the conventional, full-length, and eight-electrode actuators in the X-axis is 20.4%, 13.5%, and 17.5% of the full scan range, respectively. The hysteresis exhibited in the Z-axis is 22%, 15.8%, and 14.7%, respectively. Reduction of hysteresis can be achieved by either open-loop [23], [24] or closed-loop methods [25], [26].

The discrepancies between the simulated and experimental results are partially due to uncertainty in d_{31}. Piezoelectric constants are estimated for small-signals and do not account for the hysteresis nonlinearity observed in Fig. 6. Significant differences in d_{31} are expected when the full voltage range is utilized [27]. The d_{31} value of the full-length configuration was found to increase from 305 to 440 pm/V when the tube is driven at -10 and -200 V, respectively.

V. Conclusion

This article proposed two new methods for driving piezoelectric tube actuators. The first method aims to maximize the lateral and vertical deflection by driving the internal electrode, which eliminates the need for a circumferential Z-electrode. Experimental results show a 62% increase in lateral scan range and an 87% increase in the vertical scan range.

A second configuration is also described with eight external electrodes and a driven internal electrode. This method is primarily aimed at eliminating the vertical motion and tilting induced by lateral deflection. Experimental results show a 96% and 62% reduction in tilting and vertical cross-coupling, respectively, and 44% increase in vertical scan range. However, the lateral scan range was also reduced by 44%.

The proposed eight-electrode configuration with driven internal electrode is recommended for applications that require maximum vertical scan range with lowest possible tilting and vertical cross-coupling. For applications where tilting is not a concern, the proposed full-length tube actuator is recommended.

References

[1] H. Zhang *et al.*, "Distributed Hammerstein modeling for cross-coupling effect of multiaxis piezoelectric micropositioning stages," *IEEE/ASME Trans. Mechatronics*, vol. 23, no. 6, pp. 2794–2804, Dec. 2018.

[2] Y. K. Yong and S. O. R. Moheimani, "Collocated z-axis control of a high-speed nanopositioner for video-rate atomic force microscopy," *IEEE Trans. Nanotechnol.*, vol. 14, no. 2, pp. 338–345, Mar. 2015.

[3] G. Gu, L. Zhu, C. Su, H. Ding, and S. Fatikow, "Modeling and control of piezo-actuated nanopositioning stages: A survey," *IEEE Trans. Autom. Sci. Eng.*, vol. 13, no. 1, pp. 313–332, Jan. 2016.

[4] S. Wadikhaye, Y. K. Yong, and S. O. R. Moheimani, "A serial-kinematic nanopositioner for high-speed AFM," *Rev. Sci. Instrum.*, vol. 85, no. 10, 2014, Art. no. 105104.

[5] Y. K. Yong and S. O. R. Moheimani, "A compact XYZ scanner for fast atomic force microscopy in constant force contact mode," in *Proc. IEEE/ASME Int. Conf. Adv. Intell. Mechatronics*, Jul. 2010, pp. 225–230.

[6] Y. K. Yong, S. O. R. Moheimani, B. J. Kenton, and K. K. Leang, "Invited review article: High-speed flexure-guided nanopositioning: Mechanical design and control issues," *Rev. Sci. Instrum.*, vol. 83, no. 12, 2012, Art. no. 121101.

[7] B. J. Kenton and K. K. Leang, "Design and control of a three-axis serial-kinematic high-bandwidth nanopositioner," *IEEE/ASME Trans. Mechatronics*, vol. 17, no. 2, pp. 356–368, Apr. 2012.

[8] D. Zhang, P. Li, J. Zhang, H. Chen, K. Guo, and M. Ni, "Design and assessment of a six-DOF micro-/nanopositioning system," *IEEE/ASME Trans. Mechatronics*, vol. 24, no. 5, pp. 2097–2107, Oct. 2019.

[9] X. Li, D. MacDonald, and M. Myaing, "Scanning fiber-optic nonlinear optical imaging and spectroscopy endoscope," U.S. Patent App. 11/623,974, Sep. 13, 2007.

[10] N. Zhang *et al.*, "Compact piezoelectric transducer fiber scanning probe for optical coherence tomography," *Opt. Lett.*, vol. 39, no. 2, pp. 186–188, Jan. 2014.

[11] S. Vilches, S. Kretschmer, C. Ataman, and H. Zappe, "Miniaturized fourier-plane fiber scanner for OCT endoscopy," *J. Micromechanics Microengineering*, vol. 27, no. 10, 2017, Art. no. 105015.

[12] R. N. Shah, S. Kretschmer, J. Nehlich, C. Ataman, and H. Zappe, "Compact OCT probe for flexible endoscopy enabled by piezoelectric scanning of a fiber/lens assembly," in *Proc. SPIE OPTO MOEMS Miniaturized Syst. XVIII*, vol. 10931, 2019. [Online]. Available: https://doi.org/10.1117/12.2508481

[13] D. Y. Kim *et al.*, "Lissajous scanning two-photon endomicroscope for *in vivo* tissue imaging," *Sci. Rep.*, vol. 9, no. 1, Mar. 2019, Art. no. 3560.

[14] F. Helmchen, M. S. Fee, D. W. Tank, and W. Denk, "A miniature head-mounted two-photon microscope: High-resolution brain imaging in freely moving animals," *Neuron*, vol. 31, no. 6, pp. 903–912, 2001.

[15] L. Li, C. Li, G. Gu, and L. Zhu, "Modified repetitive control based cross-coupling compensation approach for the piezoelectric tube scanner of atomic force microscopes," *IEEE/ASME Trans. Mechatronics*, vol. 24, no. 2, pp. 666–676, Apr. 2019.

[16] S. O. R. Moheimani, "Invited review article: Accurate and fast nanopositioning with piezoelectric tube scanners: Emerging trends and future challenges," *Rev. Sci. Instrum.*, vol. 79, no. 7, 2008, Art. no. 071101.

[17] Y. K. Yong, B. Ahmed, and S. O. R. Moheimani, "Atomic force microscopy with a 12-electrode piezoelectric tube scanner," *Rev. Sci. Instrum.*, vol. 81, no. 3, 2010, Art. no. 033701.

[18] W. S. Bacsa, "Optical interference near surfaces and its application in subwavelength microscopy," in *Proc. Adv. Imag. Electron. Phys.*, 2010, vol. 163, pp. 1–32.

[19] M. Hannss, W. Naumann, and R. Anton, "Performance of a tilt-compensating tube scanner in atomic force microscopy," *Scanning*, vol. 20, no. 7, pp. 501–507, 1998.

[20] D. G. Fertis, *Nonlinear Structural Engineering: With Unique Theories and Methods to Solve Effectively Complex Nonlinear Problems*. Berlin, Germany: Springer Science & Business Media, 2007.

[21] C. J. Chen and C. Julian, "Electromechanical deflections of piezoelectric tubes with quartered electrodes," *Appl. Phys. Lett.*, vol. 60, no. 1, pp. 132–134, 1992.

[22] J. Maess, A. J. Fleming, and F. Allgöwer, "Simulation of dynamics-coupling in piezoelectric tube scanners by reduced order finite element analysis," *Rev. Sci. Instrum.*, vol. 79, no. 1, 2008, Art. no. 015105.

[23] Z. Li and J. Shan, "Modeling and inverse compensation for coupled hysteresis in piezo-actuated Fabry-Perot spectrometer," *IEEE/ASME Trans. Mechatronics*, vol. 22, no. 4, pp. 1903–1913, Aug. 2017.

[24] A. J. Fleming, "Quantitative SPM topographies by charge linearization of the vertical actuator," *Rev. Sci. Instrum.*, vol. 81, no. 10, 2010, Art. no. 103701.

[25] L. Li, C. Li, G. Gu, and L. Zhu, "Modified repetitive control based cross-coupling compensation approach for the piezoelectric tube scanner of atomic force microscopes," *IEEE/ASME Trans. Mechatronics*, vol. 24, no. 2, pp. 666–676, Apr. 2019.

[26] R. de Rozario, A. J. Fleming, and T. Oomen, "Finite-time learning control using frequency response data with application to a nanopositioning stage," *IEEE/ASME Trans. Mechatronics*, vol. 24, no. 5, pp. 2085–2096, Oct. 2019.

[27] A. J. Fleming and Y. K. Yong, "An ultrathin monolithic XY nanopositioning stage constructed from a single sheet of piezoelectric material," *IEEE/ASME Trans. Mechatronics*, vol. 22, no. 6, pp. 2611–2618, Dec. 2017.

Digvijay S. Raghunvanshi received the bachelor of mechanical engineering degree from the Bharati Vidyapeeth University, Pune, India, in 2012, and the master's degree in electrical engineering from the University of Newcastle, Callaghan, NSW, Australia, in 2018.

He is currently working in the Australian Telecom sector with NBN Co. projects. His research interests include design and analysis of mechatronic devices, and optimization of resources and processes.

Steven I. Moore received the bachelor of electrical engineering and bachelor of mathematics degrees, in 2012, and the Ph.D. degree in electrical engineering, in 2016, from the University of Newcastle, Callaghan, NSW, Australia.

He is currently a Postdoctoral Researcher with the Precision Mechatronics Lab with the University of Newcastle. His research interests include design, modeling, implementation, and optimization of mechatronic systems including precision motion control and sensing in microelectromechanical systems (MEMS), structural design of piezoelectric microcantilevers, nanopositioning, ultrahigh bandwidth fixed point control realizations, image stabilization in optical systems, and inertial stabilization systems.

Andrew John Fleming (Member, IEEE) received the bachelor of electrical engineering, in 2000, and Ph.D. degree in electrical engineering, in 2004, from The University of Newcastle, Australia, Callaghan, NSW, Australia.

He is currently the Director of the Priority Research Center for Complex Dynamic Systems and Control and the Precision Mechatronics Lab (www.pmtxlab.com) at The University of Newcastle, Australia. He is the coauthor of three books and more than 200 journal and conference articles. His research interests include lithography, nanopositioning, scanning probe microscopy, and biomedical devices.

Dr. Fleming's research awards include the IEEE MARSS Best Paper Award in 2019, ATSE Baterham Medal in 2016, IEEE Control Systems Society Outstanding Paper Award in 2007, The University of Newcastle Researcher of the Year Award in 2007. He is the inventor of several patent applications, and in 2012 he received the Newcastle Innovation Rising Star Award for Excellence in Industrial Engagement.

Yuen Kuan Yong (Member, IEEE) received the bachelor of engineering degree in mechatronics engineering and the Ph.D. degree in mechanical engineering from The University of Adelaide, Australia, in 2001 and 2007, respectively.

She was an Australian Research Council DECRA Fellow, from 2013 to 2017. She is currently an Associate Professor with the School of Electrical Engineering and Computing, the University of Newcastle, Callaghan, NSW, Australia. Her research interests include nanopositioning systems, design and control of novel microcantilevers, atomic force microscopy, and soft robotics.

Dr. Yong is the recipient of the IEEE MARSS Best Paper Award in 2019, the University of Newcastle Vice-Chancellor's Award for Research Supervision Excellence, in 2017, and the Vice-Chancellor's Award for Research Excellence, in 2014. She is an Associate Editor for the IEEE/ASME TRANSACTIONS OF MECHATRONICS.